Accepted manuscript

Efficient vacuum deposited *p-i-n* and *n-i-p* perovskite solar cells employing doped charge transport layers

Cristina Momblona[1,‡], Lidón Gil-Escrig[1,‡], Enrico Bandiello[1], Eline M. Hutter[2], Michele Sessolo[1], Kay Lederer[3], Jan Blochwitz-Nimoth[3]* and Henk J. Bolink[1]*

[1]Instituto de Ciencia Molecular, Universidad de Valencia, C/ Catedrático J. Beltrán 2, 46980 Paterna (Valencia), Spain

[2]Department of Chemical Engineering, Delft University of Technology, Van der Maasweg 9, 2629 HZ Delft, the Netherlands

[3]NOVALED GmbH, Tatzberg 49, 01307 Dresden, Germany

*Correspondence to: jan.bn@novaled.com and henk.bolink@uv.es

‡These authors contributed equally to this work

Thin-film photovoltaics is a promising technology for low-cost and sustainable renewable energy sources. Organic-inorganic (hybrid) lead halide perovskite solar cells have recently aroused wide interest in photovoltaic applications because of their impressive power conversion efficiencies (PCEs), now exceeding 21%.[1-3] Importantly, the perovskite thin-film absorber can be deposited using low-cost and abundant starting materials, hence with a large potential for the preparation of inexpensive photovoltaic devices.[4] The high PCEs are the result of the very high absorption coefficient and mobilities of the photogenerated electrons and holes

of hybrid perovskites.[5, 6] While the use of the archetype perovskite, methylammonium lead iodide ($MAPbI_3$), can lead to high efficiency devices,[7, 8] a further decrease of the bandgap by incorporation of formamidinium (FA), allows for the harvesting of additional near-infrared photons.[9] When such a mixed organic cation perovskite is further stabilized by replacing part of the iodide with bromide, and/or by partial cesium incorporation, the champion materials for perovskite cells are obtained.[3, 10-12] Two main solar cell architectures have been used so far. One of them derives from dye-sensitized solar cells, and consists of a transparent conductive substrate coated with a mesoporous/planar TiO_2 layer (n-type, hence acting as the electron transport layer, ETL) into/onto which the perovskite absorber is applied.[13-15] A hole transport layer (HTL, p-type), usually consisting of organic semiconductors is then deposited on top of the perovskite and the device is finished with an evaporated top electrode. The second common configuration is inverted compared to the one mentioned above, and the conductive substrate is coated with a HTL, followed by the perovskite absorber and an ETL, coated with a suitable evaporated top electrode.[16, 17] While in the perovskite solar cells literature these two device configurations have been referred to as "conventional" and "inverted", a less confusing nomenclature, *n-i-p* and *p-i-n*, will be used throughout this manuscript. Recently, Chen et al. demonstrated that the PCE in planar devices can be improved by increasing the conductivity of the metal oxide layers by incorporating heteroatoms with different valences.[18] The increase in the conductivity was limited, however (approximately one order of magnitude), limiting the thickness of the metal oxide layers to 20 nm. An alternative strategy to improve the conductivity of charge transport layers is the use of doped organic semiconductors. These materials have been widely studied for organic light-emitting diodes (OLEDs) and small molecular weight organic solar cells (OPVs). In these applications they have proven to enhance charge carrier injection and transport, and more manufacturing oriented properties as large area uni-

formity and yield.[19-21] In doped organic semiconductors the conductivity can be varied over several orders of magnitude by varying the doping concentration, yet without an associated strong increase in the optical absorption of the layer. This is advantageous because it allows the use of rather thick (100 nm) doped layers generating additional freedom to design/fine-tune the device architecture.

Most reported solar cells using a vacuum deposited perovskite layer still employ charge transport layers processed from solution.[22-24] Fully vacuum deposited perovskite devices would offer the additional advantage of being compatible with temperature sensitive substrates, allowing for conformal coatings on non-planar substrates and for the straightforward implementation into tandem solar cells.[25] Additionally, vacuum processing is an established technique in the electronic industry demonstrating high throughput and reliability.[26] In principle, solution processing of semiconductor can be an inexpensive alternative to vacuum deposition, however, the impact of the processing costs is very limited on the overall module price, which is dominated by the material cost. Polander et. al., were the first to demonstrate fully vacuum deposited cells where open circuit voltages (V_{oc}) as high as 1.1 V were obtained.[27] The highest efficiency (15.4%) reported for fully vacuum deposited perovskite solar cells were inferred from a device with rather high hysteresis, which used undoped organic molecules as the charge extraction materials.[28, 29]

Here, we present fully vacuum deposited planar perovskite solar cells in which the perovskite layer is sandwiched in between two charge extraction double-layers. The latter consist of a thin layer of pristine organic charge transport molecules and a thicker layer consisting of the same molecules that are partially oxidized (in the case of the hole transporter) or reduced (in the case of the electron transport layer). The partial oxidation or reduction of the charge

transport molecules leads to p- and n-type doped layers, respectively, with a significantly enhanced conductivity. These multi-layer solar cells have been prepared in both the *p-i-n* and *n-i-p* architectures, allowing for a direct comparison between these two designs. We demonstrate that the presence of thin undoped layers is beneficial for the device performance. Average power conversion efficiencies of 15% and 18% are obtained for the *p-i-n* and *n-i-p* architectures, respectively, bringing vacuum deposited perovskite solar cells closer to their solution-processed equivalent.

The $MAPbI_3$ perovskite thin films were prepared by co-evaporation of the two starting compounds, CH_3NH_3I and PbI_2. Details of the experimental conditions for the perovskite layer have been described previously and are presented in the supporting information.[23] Out of the two perovskite precursors, CH_3NH_3I and PbI_2 the first is somewhat complicated to sublime. However, once properly outgassed (using the high vacuum of the evaporation chamber) the material is sublimed similarly like small molecular weight organic molecules, that is, the rate of evaporation is stable as monitored by the microbalance crystal sensors that are positioned in the chamber. These films were characterized using grazing incidence X-ray diffraction (GIXRD) showing the typical diffraction pattern for this material which is independent on the type of under-layer employed (Fig. S1a in the ESI†). Scanning electron microscopy (SEM) images both of the perovskite surface (Fig. S1b in the ESI†) and of the device cross-section (Fig. 1) show a dense packing of crystals, virtually without any pinholes, that have an average domain size of approximately 100 nm. The surface is homogeneous and smooth with roughness (root mean square), estimated by atomic force microscopy over an area of 25 μm^2, of only 10.1 nm (Fig. S2 in the ESI†). The optical absorption spectra of these films show the expected $MAPbI_3$ band-to-band transition at 780 nm and high absorbance over the whole visible spectra (Fig. S1c in the ESI†). The perovskite film formation is very reproducible and the

layer properties did not change over a period of 6 months during which the experiments described in this manuscript were performed. These perovskite layers were used to prepare planar diodes by sandwiching a 500 nm thick perovskite layer in between organic HTLs and ETLs, initially, the first on top of a pre-patterned indium tin oxide (ITO) coated glass substrate and by thermally evaporating a metal top contact on the latter. A vacuum evaporated $MAPbI_3$ layer of 500 nm was selected as it was shown that almost all sub-bandgap sun light is absorbed and still all charge carriers can reach the respective interfaces.[30] Both organic charge transport layers were prepared by vacuum sublimation of the corresponding organic molecules to a layer thickness of 10 nm. As the hole transport molecule we selected a derivative of an arylamine, N4,N4,N4",N4"-tetra([1,1'-biphenyl]-4-yl)-[1,1':4',1"-terphenyl]-4,4"-diamine (TaTm) (Fig. 1) due to its very stable sublimation conditions and tendency to form completely amorphous films. The fullerene C_{60} was selected as the electron transport molecule as it is also easy to sublime and has proven to be an efficient electron acceptor in perovskite solar cells.[29, 31] To ensure sufficient statistics, for each device configuration mentioned in this report, at least 2 different devices each containing 4 cells were evaluated, while for top performing configurations at least 5 different devices with a total of 20 cells were characterized. The device area used, defined as the aperture of the shadow mask, was 1 mm^2 and for top performing devices, larger areas of 10, 27 and 85 mm^2 were also used.

Using the architecture described above, employing single layers of hole and electron extraction molecules (without any electrical dopant), the photovoltaic performance of the diodes under 1 sun illumination was rather poor, due to a pronounced s-shape of the current density (J) versus voltage (V) curve, leading to poor fill factors (FF) and hence low PCE values (Fig. S3 and Table S1, in the ESI†). This indicates that the charge carrier's extraction is severely hindered, either due to the high resistance of the organic charge transport layers or to the pres-

ence of an extraction barrier at the electrode interfaces. To reduce the series resistance of the charge transport layers and to ensure an ohmic contact between them and the electrodes we prepared partially oxidized and reduced HTL and ETL, respectively, by co-evaporation of the charge transport molecules with a suitable reactant (see Fig. 1). This method allows for a precise control of the ratios of each molecule in the sublimed film by carefully monitoring the evaporation rate using micro-balance sensors during the evaporation process. These partially oxidized and reduced hole and electron transport layers are referred to as "doped" charge transport layers. Here we selected molecular dopants due to their intrinsic advantages over inorganic reactants,[32] i.e. the molecular dopants typically evaporate at a suitable temperature range between 100 °C and 400 °C, are less prone to oxidation when handling in air and are more diffusion stable inside the organic layers. For the HTL we used 2,2′-(perfluoronaphthalene-2,6-diylidene) dimalononitrile (F_6-TCNNQ) as the organic dopant whereas for the C_{60} ETL, N1,N4-bis(tri-p-tolylphosphoranylidene) benzene-1,4-diamine (PhIm) (Fig. 1) was employed. In OPVs, the presence of a thin layer of the pure, undoped charge transport molecule in between the doped layers and the light-absorber is often found to be beneficial. Therefore, we used this device architecture (Fig. 1) as the starting point to study the effect of the dopant concentration on the device performance.

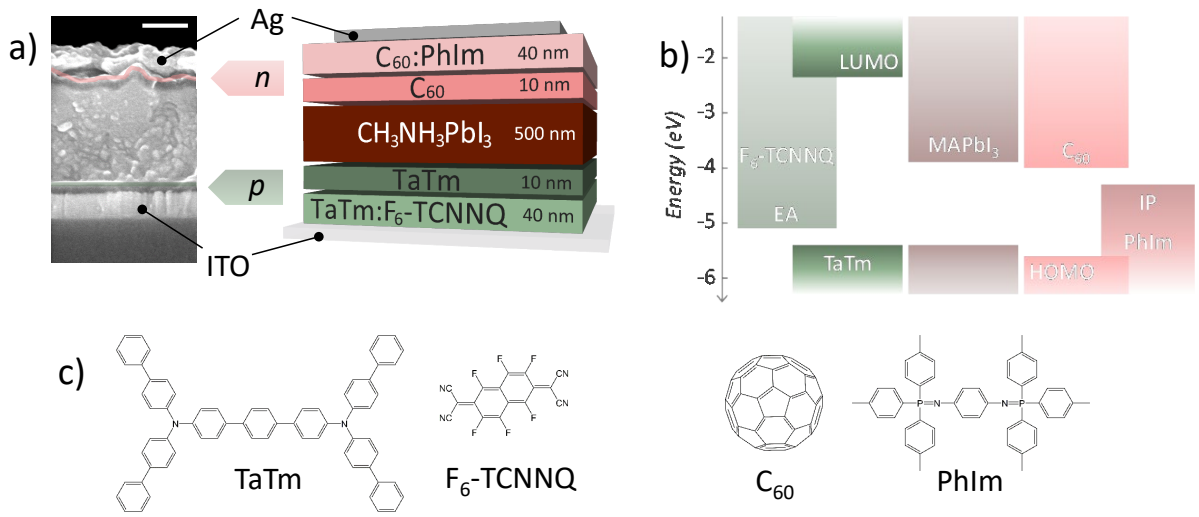

Fig. 1 (a) SEM cross-section and schematics of a completed *p-i-n* solar cell (scale bar 200 nm). (b) Flat band energy diagrams of the materials employed (the electron affinity, EA, and ionization potential, IP, of the dopants are also reported). (c) Chemical structures of the organic molecules used to prepare the charge transport layers.

To verify the optimum dopant concentration in the p-HTL we first kept the dopant concentration in the n-ETL constant at 30 wt.%. The main effect of an increasing F_6-TCNNQ concentration is the increase in the *FF* from 55% for a F_6-TCNNQ concentration of 3 wt.% to a maximum of 74% at a F_6-TCNNQ concentration of 11 wt.%. This trend reflects the increased conductivity of the p-HTL for increasing doping levels, as measured by depositing the co-evaporated films on interdigitated electrodes (Fig. S4 in the ESI†). Hence, charges are extracted more efficiently as the p-HTL conductivity increases. The open circuit voltage (V_{oc}) increases as well with increasing F_6-TCNNQ concentration going from 1053 mV to 1082 mV. This effect is likely to be a consequence of a reduction in the charge recombination due to the more efficient charge carrier extraction from the perovskite to the external contacts. The

short-circuit current density (J_{sc}), however, decreases when the F_6-TCNNQ concentration is increased. This is due to the higher absorbance of the p-HTL (Fig. S5 in the ESI†), diminishing the light intensity reaching the perovskite absorber and hence decreasing the device EQE (Fig. 2a).

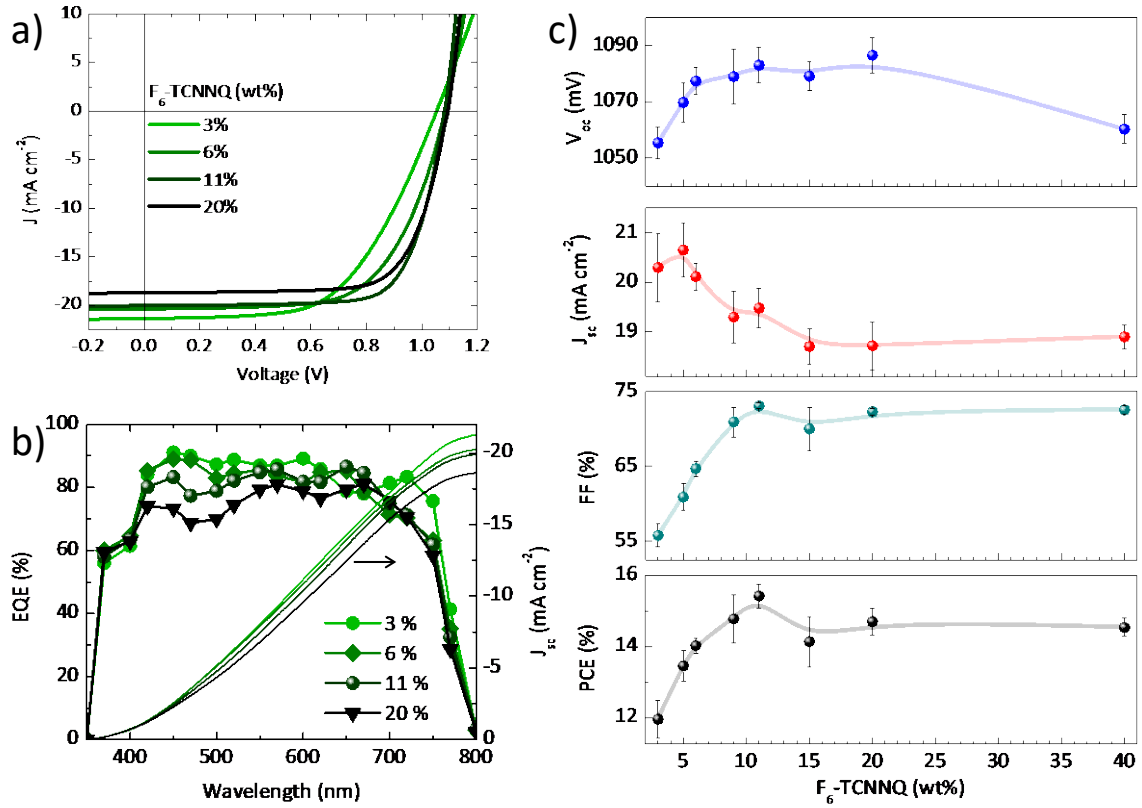

Fig. 2 (a) *J-V* curves under100 mW cm^{-2} illumination and (b) external quantum efficiency (EQE) as a function of F_6-TCNNQ concentration (the integrated photocurrent with the AM1.5G solar spectrum is shown on the right axis). (c) Evolution of the key parameters deduced from the *J-V* curves, V_{oc}, J_{sc}, *FF* and PCE, as a function of F_6-TCNNQ concentration.

Due to this reduction in J_{sc} we found an optimum in the average PCE of 15.4 % at a F_6-TCNNQ concentration of 11 wt. %. Once established the optimum dopant concentration in the p-HTL at 11 wt.%, the amount of dopant in the n-ETL was varied. The effect of the dopant concentration in the n-ETL on the photovoltaic performance is not very pronounced (Fig. S6a in the ESI†). This indicates that in the dopant range studied, the conductivity of the n-ETL is sufficiently high to ensure an efficient electron extraction to the electrodes. Indeed, even for rather low PhIm concentrations, the conductivity of the n-ETL is already higher than that of the p-HTL (Fig. S4 in the ESI†) which supports this assumption. Importantly, the efficiency of the p-i-n devices is essentially unvaried (we observe only a small reduction of the FF) when the thickness of the doped transport layers is increased from 40 to 90 nm (Fig. S6b in the ESI†).

One of the benefits of vacuum deposition is the insensitivity towards the substrate to be coated, which allows to prepare inverted devices (*n-i-p*) using the same materials and layers as described above, simply be evaporating them in the reverse order. The only difference is the top metal electrode, Ag for the *p-i-n* cells and Au for the *n-i-p* cells (Au was used for its higher work function). The *n-i-p* devices are particularly interesting as up to now most perovskite solar cells in this configuration employ metal oxides as the ETL, and only very few reports used a purely organic electron acceptor below the perovskite layer.[29]

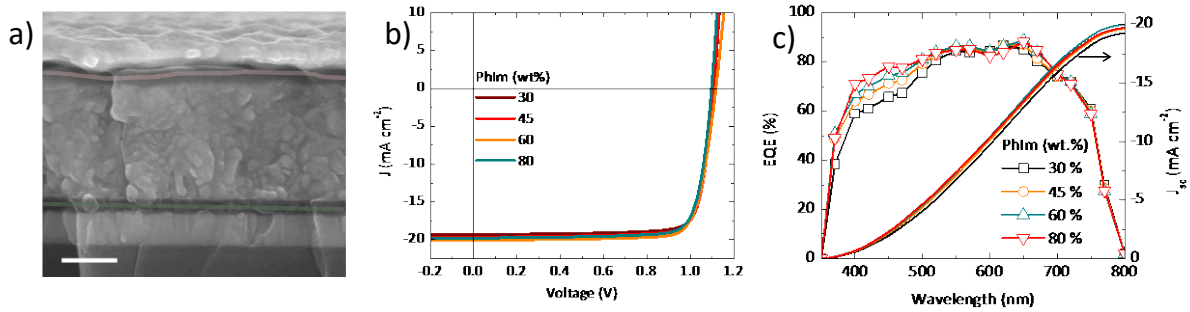

Fig. 3 (a) Cross-sectional SEM image of a completed *n-i-p* solar cell (scale bar 200 nm). (b) *J-V* curves under 100 mW cm^{-2} illumination and (c) EQE spectra (the integrated photocurrent with the AM1.5G solar spectrum is shown on the right axis) as a function of PhIm concentration.

In Fig. 3, a cross-sectional SEM image of a completed *n-i-p* solar cell is depicted, showing a dense perovskite layer with low roughness and the conformal coating of the thin organic charge transport layers. The *J-V* characteristics under 100 mW cm^{-2} illumination employing a fixed F_6-TCNNQ concentration of 11 wt.% in the p-HTL and with varying PhIm (n-dopant) concentrations are shown in Fig. 3b. The J_{sc} increases slightly with increasing PhIm content and reaches an average of 20 mA cm^{-2} for the highest n-dopant concentration. This is a consequence of the reduced C_{60} content and subsequent reduced optical absorbance of the n-ETL (Fig. S5b in the ESI†), here used as the front contact. The higher transmittance is also the origin of the observed increase in EQE with increasing PhIm content (Fig. 3c). The V_{oc} and *FF* do not change significantly in the n-dopant range evaluated, maintaining values as high as 1.1 V and 80 %, respectively. These parameters lead to PCEs of 18% on average (Fig. S7 in

the ESI†) with one pixel exceeding 20% for the record *n-i-p* cell (Fig. S8 in the ESI†) obtained with a PhIm concentration of 60 wt.%. These efficiency values might be surprising considering the rather small crystal size observed in our $MAPbI_3$ thin films (50-200 nm), and somehow contradict the accepted view on the need of large crystals in order to have long charge diffusion length and efficient charge collection.[33] Hence, we estimated the charge carrier diffusion length by means of time resolved microwave conductivity (TRMC) measurements on $MAPbI_3$ films deposited on quartz substrates (see ESI† for details on the characterization). The samples were illuminated with a 650 nm laser, and the excitation intensity was tuned in order to obtain a charge concentration of approximately 10^{15} cm^{-3}, which is comparable to excitation under standard AM1.5 illumination.[34] In this conditions, the effective mobility was determined to be 3.9 cm^2 $(Vs)^{-1}$, with a half lifetime of 210 ns (Fig. S9 in the ESI†). Considering these parameters, the charge carrier diffusion length is determined to be ~1.5 μm, in agreement with previous estimations on solution-processed $MAPbI_3$ films.[35, 36] Besides the impact of the grain size on the carrier diffusion length, the nature of grain boundaries and defects in perovskite will have a substantial influence as well. Many reports have highlighted that grain boundaries in perovskite are substantially benign, since they do not generate any states within the bandgap of $MAPbI_3$.[37] Such effects might be responsible for the high charge diffusion length observed here, leading to efficient solar cells even with perovskite films composed by relatively small crystals.

Motivated by the high PCE obtained for the *n-i-p* devices, a series of cells with increasing area (for both the electrode overlap and the shadow mask aperture, see the Experimental part in the ESI† for details) was prepared. The *FF* decreases with increasing area, causing the PCE to drop from 19.7 % to 15.0 % when going from 0.1 to 0.85 cm^2 (Fig. S10 in the ESI†), in agreement with similar larger cells.[18] The performance of the *n-i-p* solar cells is strongly

improved compared to that of the devices in the *p-i-n* configuration (Fig. S7 in the ESI†), primarily due to an increase in the *FF*, which is above 80% regardless of the PhIm concentration (Fig. S11b in the ESI†). The reason for the enhanced *FF,* when going from the *p-i-n* to the *n-i-p* configuration, is probably related to the difference in conductivity of the doped charge transporting layers at the front contact. The n-ETL conductivity is two orders of magnitude higher compared to the p-HTL, for the different dopant concentrations evaluated (Fig. S4 in the ESI†). The *FF* of *p-i-n* cells increases at lower light intensities, even for cells using the optimum 11 wt.% dopant concentration. Yet, in contrast in *n-i-p* devices, the effect of the PhIm dopant concentration on the *FF* is present only at low illumination intensity, becoming virtually concentration independent when the light intensity increases (Fig. S11a,b in the ESI†). This therefore, confirms that in the *p-i-n* configuration a barrier for hole extraction exists, in agreement also with recent estimation of the carrier collection efficiency on vacuum deposited perovskite cells (using solution processed charge transport layers).[38] Those devices, besides showing PCEs of approximately 15 % (similar to the p-i-n cells presented here), suffered from hindered and spatially inhomogeneous charge transport, which was suggested to be at the front contact, i.e. at the hole transport interface. Measurements of the electroluminescence of *p-i-n* devices (Fig. S11c,d in the ESI†) shows that the radiant flux saturates at about 1.7 V and then starts to decrease, whereas the *n-i-p* devices show enhanced electroluminescence with no saturation. This confirms a more efficient and balanced charge carrier injection which translate in higher *FF* for the n-i-p devices. The ability to efficiently inject holes when the doped p-HTL is placed in between the HTL and the metal electrode (as in *n-i-p* devices) can be understood considering that the metal electrode is evaporated on top of the p-HTL which leads to an improved contact (metal atoms slightly penetrate the soft organic layer) and potentially to an increased conductivity. It is worth to mention that the EQE for electrolumi-

[12, 32] Very small hysteresis between forward (negative to positive bias) and reverse *J-V* scans was observed only for *p-i-n* devices (Fig. S13a in the ESI†), where small fluctuations in the V_{oc} and *FF* were present due to the extraction issues at the ITO/p-HTL contact (the overall variation of the PCE was limited to 0.1%). On the other hand, *n-i-p* devices were essentially hysteresis-free, independently on the scan speed used (Fig. S13b and Table S2 in the ESI†).

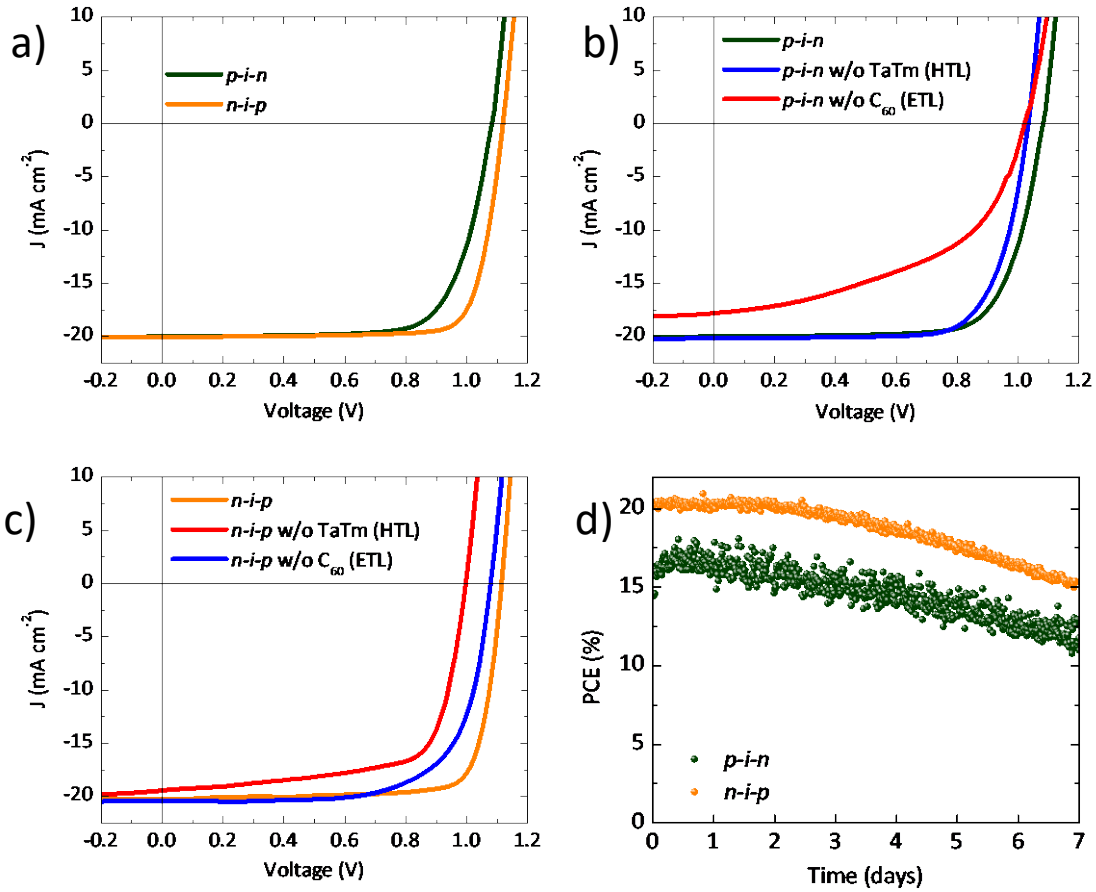

Fig. 4 (a) *J-V* curves for *n-i-p* and *p-i-n* solar cells under 100 mW cm^{-2} illumination. (b) *J-V* curves under 100 mW cm^{-2} illumination for *p-i-n* devices without one of the undoped charge

transport layers. (c) *J-V* curves under 100 mW cm^{-2} illumination for *n-i-p* devices without one of the undoped charge transport layers. (d) Stability under approximated 100 mW cm^{-2} illumination.

The initial device configuration with undoped HTL and ETL in between the perovskite and the doped charge transport layers was chosen to prevent any negative interaction between the radical cations and anions that are present in the doped charge transport layers, and the photogenerated charge carriers in the perovskite. However, it is not obvious whether such a negative interaction in fact occurs, since in perovskites electrons and holes are spontaneously formed after photon absorption without long living intermediate excitonic states and, additionally, the absorber layer is very thick compared with the organic photovoltaic devices. Therefore, two series of devices without the undoped interlayers were prepared and evaluated; the first, without the undoped HTL and a second without the undoped ETL. We first examined the *p-i-n* configuration, where the dopant concentrations were fixed at the optimum 11 and 30 wt.% for the p-HTL and n-ETL, respectively. In Fig. 4b, the *J-V* curves of these two series of devices are compared with the reference cell in which both undoped layers are present. The performance of the devices without the undoped ETL is significantly worse than the reference cell, due to a lower J_{sc}, V_{oc} and, most pronounced, a lower *FF*. Without the C_{60} ETL, the perovskite film is in direct contact with the conductive doped n-ETL, therefore electron-hole recombination can occurs at this interface causing the simultaneous reduction of all the performance indicators of the solar cells. In contrast, the cells without the undoped TaTm HTL perform only slightly worse compared to the reference cells, with a small reduction in the J_{sc} and V_{oc}. Most likely, due to the low dopant content and hence low conductivity of the p-HTL

(when compared to the n-ETL), this layer can still efficiently confine the electrons in the perovskite absorber and inhibit charge recombination at the p-HTL/$MAPbI_3$ interface. The slight decrease in V_{oc} observed upon removal of the non-doped TaTm layer can be attributed to the lower Fermi level of the p-HTL compared to the highest occupied molecular orbital (HOMO) of the TaTm. Additionally, we have studied also the effect of the selective removal of one of the doped organic layers on the device performances. As clearly observed in Fig. S14 (ESI†), both doped p-HTL and n-HTL are required to avoid severe charge extraction issues. However, and in accordance with previous reports,[23, 24] devices with only a thin layer of pure C_{60} and no doped layer between the fullerene and the metal show lower (*FF* especially) but still appreciable photovoltaic behavior. This effect originates from the interface dipole which is created at the interface between noble metals (Au and, as in our case, Ag) and C_{60}, enhancing electron extraction.[39] Also in the *n-i-p* configuration the effect of the undoped charge transport layers was evaluated. Fig. 4c shows the *J-V* characteristics for the cells without one of the undoped charge transport layers and the reference *n-i-p* cell. As observed in the p-i-n configuration, the removal of the undoped layers leads to a decrease in device performance. The effect of the removal of the C_{60} in between the n-ETL and the perovskite substantially reduces the V_{oc} and FF, while the removal of the undoped HTL, has a limited effect on the device performance, in agreement with what was observed for *p-i-n* devices and with the conductivity trend among the p-HTL and the n-ETL. Hence, independently on the device configurations, the presence of the undoped layers in between the perovskite and the doped charge transport layers is required for high efficiency cells.

To obtain an indication of the stabilities of the different cell configurations they were analyzed during prolonged exposure to white LED light (spectra in Fig. S15 in the ESI†). The light intensity was adjusted by setting the J_{sc} of the solar cells equal to the value obtained un-

der 1.5 AM illumination. The temperature of the cells during this test reached approximately 40 °C in the first 10 minutes and remained constant afterwards in part due to the LED lights used that radiate less hear than incandescent lamps. The setup consisted of 8 test positions installed inside a nitrogen filled glovebox (with oxygen and H_2O levels below 1 ppm). All cells were illuminated under short-circuit conditions without encapsulation and positioned within a few days after preparation. At fixed time intervals *J-V* scans were taken to deduce the key performance indicators of the cells (Fig. S16 in the ESI†) from which the evolution of the PCE was derived (Fig. 4d). From our first indicative analysis on the stability, it appears that no substantial difference in PCE lifetime exists among the *p-i-n* and *n-i-p* configurations. However, the parameters causing the PCE decay in *p-i-n* cells is the current density, which monotonically diminishes during the measured time span, while the performance degradation observed in *n-i-p* devices is caused mainly by the decrease of the *FF*. Interestingly, a lower PhIm doping concentration in the n-ETL of *n-i-p* cells was observed to partially stabilize the cell performance (Fig. S17 in the ESI†). Further optimization of the dopant and charge transport molecules and their ratios is expected to lead to improved stabilities, in analogy to what is obtained in OLEDs and organic small molecular weight PV modules. The implementation of modified perovskite absorbers with slightly lower bandgap is expected to further enhance the device PCE.

Conclusions

We have demonstrated fully vacuum deposited perovskite solar cells by depositing methylammonium lead iodide in between intrinsic and doped organic charge transport molecules. Two configurations, one inverted with respect to the other, *p-i-n* and *n-i-p*, are prepared and

optimized leading to planar solar cells without hysteresis and high efficiencies, 15% and 18% on average, respectively. It is the first time that a direct comparison between these two opposite device configuration has been reported. These fully vacuum deposited solar cells, allow to fine tune the device properties by controlling at will the individual layer thicknesses and composition for specific applications including tandem configurations.

Acknowledgements

We are grateful to Jorge Ferrando for his assistance with the sample characterization. European Union H2020 project INFORM (grant 675867), the Spanish Ministry of Economy and Competitiveness (MINECO) via the Unidad de Excelencia María de Maeztu MDM-2015-0538 and MAT2014-55200, PCIN-2015-255 and the Generalitat Valenciana (Prometeo/2012/053). C. M., E.B. and M.S. thank the MINECO for their pre- and post-doctoral (JdC) contracts.

References

1. A. Kojima, K. Teshima, Y. Shirai and T. Miyasaka, *Journal of the American Chemical Society*, 2009, **131**, 6050-6051.
2. M. M. Lee, J. Teuscher, T. Miyasaka, T. N. Murakami and H. J. Snaith, *Science*, 2012, **338**, 643-647.
3. W. S. Yang, J. H. Noh, N. J. Jeon, Y. C. Kim, S. Ryu, J. Seo and S. I. Seok, *Science*, 2015, **348**, 1234-1237.
4. J. Berry, T. Buonassisi, D. A. Egger, G. Hodes, L. Kronik, Y.-L. Loo, I. Lubomirsky, S. R. Marder, Y. Mastai, J. S. Miller, D. B. Mitzi, Y. Paz, A. M. Rappe, I. Riess, B.

Rybtchinski, O. Stafsudd, V. Stevanovic, M. F. Toney, D. Zitoun, A. Kahn, D. Ginley and D. Cahen, *Advanced Materials*, 2015, **27**, 5102-5112.
5. S. D. Stranks, G. E. Eperon, G. Grancini, C. Menelaou, M. J. P. Alcocer, T. Leijtens, L. M. Herz, A. Petrozza and H. J. Snaith, *Science*, 2013, **342**, 341-344.
6. D. Shi, V. Adinolfi, R. Comin, M. Yuan, E. Alarousu, A. Buin, Y. Chen, S. Hoogland, A. Rothenberger, K. Katsiev, Y. Losovyj, X. Zhang, P. A. Dowben, O. F. Mohammed, E. H. Sargent and O. M. Bakr, *Science*, 2015, **347**, 519-522.
7. C. Roldan-Carmona, P. Gratia, I. Zimmermann, G. Grancini, P. Gao, M. Graetzel and M. K. Nazeeruddin, *Energy & Environmental Science*, 2015, **8**, 3550-3556.
8. Y. Shao, Y. Yuan and J. Huang, *Nature Energy*, 2016, **1**, 15001.
9. N. Pellet, P. Gao, G. Gregori, T.-Y. Yang, M. K. Nazeeruddin, J. Maier and M. Grätzel, *Angewandte Chemie International Edition*, 2014, **53**, 3151-3157.
10. N. J. Jeon, J. H. Noh, W. S. Yang, Y. C. Kim, S. Ryu, J. Seo and S. I. Seok, *Nature*, 2015, **517**, 476-480.
11. M. Saliba, T. Matsui, J.-Y. Seo, K. Domanski, J.-P. Correa-Baena, N. Mohammad K, S. M. Zakeeruddin, W. Tress, A. Abate, A. Hagfeldt and M. Gratzel, *Energy & Environmental Science*, 2016, DOI: 10.1039/C5EE03874J.
12. D. Bi, W. Tress, M. I. Dar, P. Gao, J. Luo, C. Renevier, K. Schenk, A. Abate, F. Giordano, J.-P. Correa Baena, J.-D. Decoppet, S. M. Zakeeruddin, M. K. Nazeeruddin, M. Grätzel and A. Hagfeldt, *Science Advances*, 2016, **2**.
13. J. Burschka, N. Pellet, S.-J. Moon, R. Humphry-Baker, P. Gao, M. K. Nazeeruddin and M. Gratzel, *Nature*, 2013, **499**, 316-319.
14. H. Zhou, Q. Chen, G. Li, S. Luo, T.-b. Song, H.-S. Duan, Z. Hong, J. You, Y. Liu and Y. Yang, *Science*, 2014, **345**, 542-546.
15. A. Mei, X. Li, L. Liu, Z. Ku, T. Liu, Y. Rong, M. Xu, M. Hu, J. Chen, Y. Yang, M. Grätzel and H. Han, *Science*, 2014, **345**, 295-298.
16. J.-Y. Jeng, Y.-F. Chiang, M.-H. Lee, S.-R. Peng, T.-F. Guo, P. Chen and T.-C. Wen, *Advanced Materials*, 2013, **25**, 3727-3732.
17. C.-G. Wu, C.-H. Chiang, Z.-L. Tseng, M. K. Nazeeruddin, A. Hagfeldt and M. Gratzel, *Energy & Environmental Science*, 2015, **8**, 2725-2733.
18. W. Chen, Y. Wu, Y. Yue, J. Liu, W. Zhang, X. Yang, H. Chen, E. Bi, I. Ashraful, M. Grätzel and L. Han, *Science*, 2015, **350**, 944-948.
19. K. Walzer, B. Maennig, M. Pfeiffer and K. Leo, *Chemical Reviews*, 2007, **107**, 1233-1271.
20. D. J. Gaspar and E. Polikarpov, *OLED Fundamentals: Materials, Devices, and Processing of Organic Light-Emitting Diodes*, CRC Press, 2015.
21. I. Salzmann and G. Heimel, *Journal of Electron Spectroscopy and Related Phenomena*, 2015, **204, Part A**, 208-222.
22. M. Liu, M. B. Johnston and H. J. Snaith, *Nature*, 2013, **501**, 395-398.
23. O. Malinkiewicz, A. Yella, Y. H. Lee, G. M. Espallargas, M. Graetzel, M. K. Nazeeruddin and H. J. Bolink, *Nat Photon*, 2014, **8**, 128-132.
24. Q. Lin, A. Armin, R. C. R. Nagiri, P. L. Burn and P. Meredith, *Nat Photon*, 2015, **9**, 106-112.
25. M. Kaltenbrunner, G. Adam, E. D. Glowacki, M. Drack, R. Schwodiauer, L. Leonat, D. H. Apaydin, H. Groiss, M. C. Scharber, M. S. White, N. S. Sariciftci and S. Bauer, *Nat Mater*, 2015, **14**, 1032-1039.
26. L. K. Ono, M. R. Leyden, S. Wang and Y. Qi, *Journal of Materials Chemistry A*, 2016, DOI: 10.1039/C5TA08963H.

27. L. E. Polander, P. Pahner, M. Schwarze, M. Saalfrank, C. Koerner and K. Leo, *APL Materials*, 2014, **2**, 081503.
28. B.-S. Kim, T.-M. Kim, M.-S. Choi, H.-S. Shim and J.-J. Kim, *Organic Electronics*, 2015, **17**, 102-106.
29. W. Ke, D. Zhao, C. R. Grice, A. J. Cimaroli, G. Fang and Y. Yan, *Journal of Materials Chemistry A*, 2015, **3**, 23888-23894.
30. C. Momblona, O. Malinkiewicz, C. Roldán-Carmona, A. Soriano, L. Gil-Escrig, E. Bandiello, M. Scheepers, E. Edri and H. J. Bolink, *APL Materials*, 2014, **2**, 081504.
31. P.-W. Liang, C.-C. Chueh, S. T. Williams and A. K. Y. Jen, *Advanced Energy Materials*, 2015, **5**, n/a-n/a.
32. A. Genco, F. Mariano, S. Carallo, V. L. P. Guerra, S. Gambino, D. Simeone, A. Listorti, S. Colella, G. Gigli and M. Mazzeo, *Advanced Electronic Materials*, 2016, **2**, n/a-n/a.
33. W. Nie, H. Tsai, R. Asadpour, J.-C. Blancon, A. J. Neukirch, G. Gupta, J. J. Crochet, M. Chhowalla, S. Tretiak, M. A. Alam, H.-L. Wang and A. D. Mohite, *Science*, 2015, **347**, 522-525.
34. M. B. Johnston and L. M. Herz, *Accounts of Chemical Research*, 2016, **49**, 146-154.
35. E. M. Hutter, G. E. Eperon, S. D. Stranks and T. J. Savenije, *The Journal of Physical Chemistry Letters*, 2015, **6**, 3082-3090.
36. R. L. Milot, G. E. Eperon, H. J. Snaith, M. B. Johnston and L. M. Herz, *Advanced Functional Materials*, 2015, **25**, 6218-6227.
37. W.-J. Yin, T. Shi and Y. Yan, *Advanced Materials*, 2014, **26**, 4653-4658.
38. G. El-Hajje, C. Momblona, L. Gil-Escrig, J. Avila, T. Guillemot, J.-F. Guillemoles, M. Sessolo, H. J. Bolink and L. Lombez, *Energy & Environmental Science*, 2016, **9**, 2286-2294.
39. S. C. Veenstra, A. Heeres, G. Hadziioannou, G. A. Sawatzky and H. T. Jonkman, *Applied Physics A*, **75**, 661-666.

Electronic Supplementary Information

Efficient vacuum deposited p-i-n and n-i-p perovskite solar cells employing doped charge transport layers

Cristina Momblona[1,†], Lidón Gil-Escrig[1,†], Enrico Bandiello[1], Eline M. Hutter[2], Michele Sessolo[1], Kay Lederer[3], Jan Blochwitz-Nimoth[3]* and Henk J. Bolink[1]*

[1]Instituto de Ciencia Molecular, Universidad de Valencia, C/ Catedrático J. Beltrán 2, 46980 Paterna (Valencia), Spain

[2]Department of Chemical Engineering, Delft University of Technology, Van der Maasweg 9, 2629 HZ Delft, the Netherlands

[3]NOVALED GmbH, Tatzberg 49, 01307 Dresden, Germany

*Corresponding author. E-mail: jan.bn@novaled.com and henk.bolink@uv.es

Experimental

Materials. Photolithographically patterned ITO coated glass substrates were purchased from Naranjo Substrates (www.naranjosubstrates.com). 2,2'-(Perfluoronaphthalene-2,6-diylidene) dimalononitrile (F6-TCNNQ), N4,N4,N4",N4"-tetra([1,1'-biphenyl]-4-yl)-[1,1':4',1"-terphenyl]-4,4"-diamine (TaTm) and N1,N4-bis(tri-p-tolylphosphoranylidene)benzene-1,4-diamine (PhIm) were provided from Novaled GmbH. Fullerene (C_{60}) was purchased from sigma Aldrich. PbI_2 was purchased from Tokyo Chemical Industry CO (TCI), and CH_3NH_3I (MAI) from Lumtec.

Device preparation. ITO-coated glass substrates were subsequently cleaned with soap, water and isopropanol in an ultrasonic bath, followed by UV-ozone treatment. They were transferred to a vacuum chamber integrated into a nitrogen-filled glovebox (MBraun, H_2O and O_2 < 0.1 ppm) and evacuated to a pressure of $1 \cdot 10^{-6}$ mbar. The vacuum chamber uses a turbomolecular pump (Pfeiffer TMH 261P, DN 100 ISO-K, 3P) coupled to a scroll pump. This system is very robust and has been used continuously for over two years. The blades of the turbomolecular pump are cleaned roughly every year after which they continue to operate. The vacuum chamber is equipped with six temperature controlled evaporation sources (Creaphys) fitted with ceramic crucibles. The sources were directed upwards with an angle of approximately 90° with respect to the bottom of the evaporator. The substrate holder to evaporation sources distance is approximately 20 cm. Three quartz crystal microbalance (QCM) sensors are used, two monitoring the deposition rate of each evaporation source and a third one close to the substrate holder monitoring the total deposition rate. For thickness calibration, we first individually sublimed the charge transport materials and their dopants (TaTm and F_6-TCNNQ, C_{60} and PhIm). A calibration factor was obtained by comparing the thickness inferred from the QCM

sensors with that measured with a mechanical profilometer (Ambios XP1). Then these materials were co-sublimed at temperatures ranging from 135-160 ºC for the dopants to 250 ºC for the pure charge transport molecules, and the evaporation rate was controlled by separate QCM sensors and adjusted to obtain the desired doping concentration. In general, the deposition rate for TaTm and C_{60} was kept constant at 0.8 Å s^{-1} while varying the deposition rate of the dopants during co-deposition. Pure TaTm and C_{60} layers were deposited at a rate of 0.5 Å s^{-1}. For the *p-i-n* configuration, 40 nm of the p-doped hole-transport layer (p-HTL, TaTm:F_6-TCNNQ) capped with 10 nm of the pure TaTm were deposited. Once completed this deposition, the chamber was vented with dry N_2 to replace the p-HTL crucibles with those containing the starting materials for the perovskite deposition, PbI_2 and CH_3NH_3I. The vacuum chamber was evacuated again to a pressure of 10^{-6} mbar, and the perovskite films were then obtained by co-deposition of the two precursors. The calibration of the deposition rate for the CH_3NH_3I was found to be difficult due to non-uniform layers and the soft nature of the material which impeded accurate thickness measurements. Hence, the source temperature of the CH_3NH_3I was kept constant at 70 ºC and the CH_3NH_3I:PbI_2 ratio was controlled off line using grazing incident x-ray diffraction by adjusting the PbI_2 deposition temperature. The optimum deposition temperatures were found to be 250 ºC for the PbI_2 and 70 ºC for the CH_3NH_3I. After deposition of a 500 nm thick perovskite film, the chamber was vented and the crucibles replaced with those containing C_{60} and PhIm, and evacuated again to a pressure of 10^{-6} mbar. The devices were completed depositing a film of pure C_{60} and one of the n-ETL (C_{60}:PhIm), with thicknesses of 10 and 40 nm, respectively. This process of exchanging crucibles was done to evaluate the effect of changes in the organic layer composition for an identical perovskite layer. In one evaporation run we can prepare 5 substrates (3 by 3 cm) each containing 4 cells. Generally, one substrate was reserved for a reference

configuration allowing to evaluate 4 variations in the transport layers per perovskite evaporation. It is also possible to prepare the complete stack without breaking vacuum as we have 6 sources available. Finally the substrates were transferred to a second vacuum chamber where the metal top contact (100 nm thick) was deposited. For *n-i-p* devices, the exact same procedure as described before was used in the inverted order.

Characterization. Grazing incident X-ray diffraction (GIXRD) pattern were collected at room temperature on an Empyrean PANanalytical powder diffractometer using the Cu Kα1 radiation. Typically, three consecutive measurements were collected and averaged into single spectra. The surface morphology of the thin films was analyzed using atomic force microscopy (AFM, Multimode SPM, Veeco, USA). Scanning Electron Microscopy (SEM) images were performed on a Hitachi S-4800 microscope operating at an accelerating voltage of 2 kV over Platinum - metallized samples. Absorption spectra were collected using a fiber optics based Avantes Avaspec2048 Spectrometer. Characterization of the solar cells was performed as follows. The external quantum efficiency (EQE) was estimated using the cell response at different wavelength (measured with a white light halogen lamp in combination with band-pass filters), where the solar spectrum mismatch is corrected using a calibrated Silicon reference cell (MiniSun simulator by ECN, the Netherlands). The current density-voltage (J-V) characteristics were obtained using a Keithley 2400 source measure unit and under white light illumination, and the short circuit current density was corrected taking into account the device EQE. The electrical characterization was validated using a solar simulator by Abet Technologies (model 10500 with an AM1.5G xenon lamp as the light source). Before each measurement, the exact light intensity was determined using a calibrated Si reference diode equipped with an infrared cut-off filter (KG-3, Schott). Importantly, no difference in the J-V characteristics was observed as a function

of evaluation method. The J-V curves were recorded between -0.2 and 1.2 V with 0.01V steps, integrating the signal for 20 ms after a 10 ms delay. This corresponds to a speed of about 0.3 V s^{-1}. Two different devices layout has been used to test the solar cells configurations, one with four equal areas (0.0653 cm^2, defined as the overlap between the ITO and the top metal contact) and measured through a shadow masks with 0.01 cm^2 aperture, and a second with increasing areas (0.0897 cm^2, 0.1522 cm^2, 0.3541 cm^2 and 0.9524 cm^2) which was characterized using a shadow mask with aperture areas of 0.0484 cm^2, 0.1024 cm^2, 0.2704 cm^2 and 0.8464 cm^2, respectively. For hysteresis study, different scan rates (0.1, 0.5 and 1 Vs^{-1}) were used, biasing the device from -0.2 to 1.2 V with 0.01 V steps and vice versa. Light intensity dependence measurements were done by placing 0.1, 1, 10, 20, 50% neutral density filters (LOT-QuantumDesign GmbH) between the light source and the device.

Photoconductance measurements. Thin films on quartz substrates were placed in a sealed resonance cavity inside an N_2-filled glovebox. The time resolved microwave conductivity (TRMC) technique was used to measure the change in microwave (8-9 GHz) power after pulsed excitation (repetition rate 10 Hz) of the $MAPbI_3$ films at 650 nm. The photoexcitation-induced change in microwave power is related to the change in conductance ΔG by a sensitivity factor K:

$$\frac{\Delta P(t)}{P} = -K\Delta G(t)$$

The rise of ΔG is limited by the width of the laser pulse (3.5 ns FWHM) and the response time of our microwave system (18 ns). The slow repetition rate of the laser of 10 Hz ensures full relaxation of all photo-induced charges to the ground state before the next laser pulse hits the sample. The product of yield Φ and mobility ($\mu_e + \mu_h$) is calculated from the maximum change in photo-conductance ΔG_{max} by:

$$\varphi\Sigma\mu = \frac{\Delta G_{max}}{I_0 \beta e F_A}$$

Here, I_0 is the number of photons per unit area per pulse, β is the ratio of the inner dimensions of the microwave cell, e the elementary charge and F_A the fraction of light absorbed by the sample at the excitation wavelength (650 nm). Before and during the photoconductance measurements, the samples were not exposed to moisture and air to prevent degradation. The charge carrier diffusion length L_D was calculate by estimating the mobility μ and the half lifetime t, using the relation:

$$L_D = \sqrt{D\tau}$$

Where $D = \sum \mu k_B T/e$, with k_B the Boltzmann constant and T the temperature.

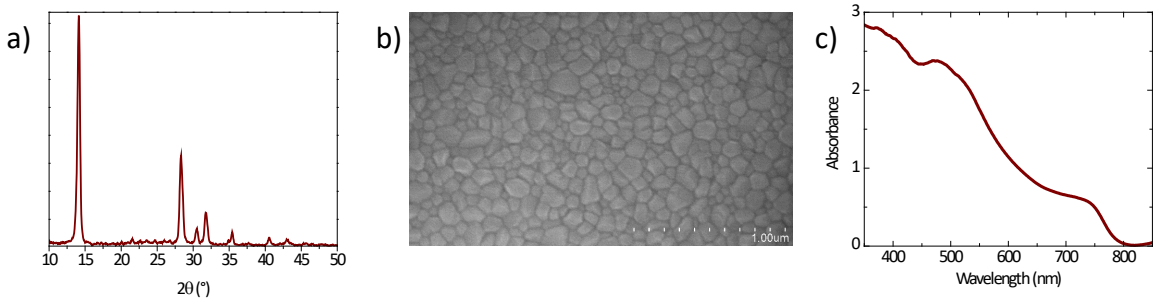

Fig. S1 (a) GIXRD pattern, (b) surface SEM picture and (c) optical absorbance of the vacuum deposited $MAPbI_3$ thin films used for *p-i-n* and *n-i-p* cells preparation.

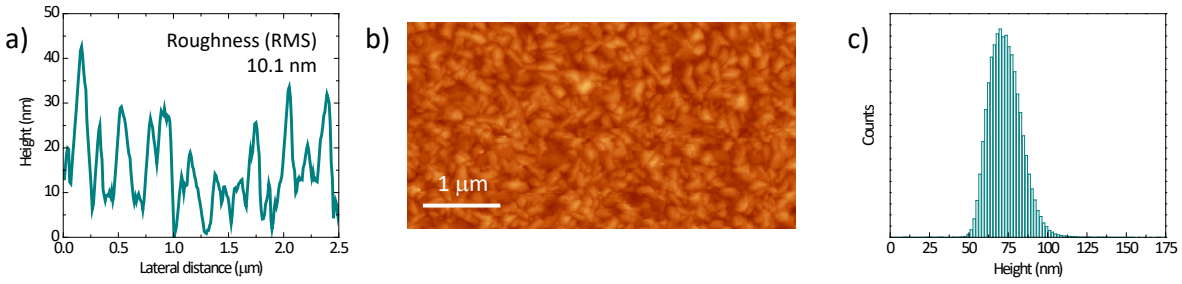

Fig. S2 Atomic force microscopy (AFM) characterization of the vacuum deposited $MAPbI_3$ thin films used for *p-i-n* and *n-i-p* cells preparation: (a) Surface profile, (b) topography and (c) roughness analysis

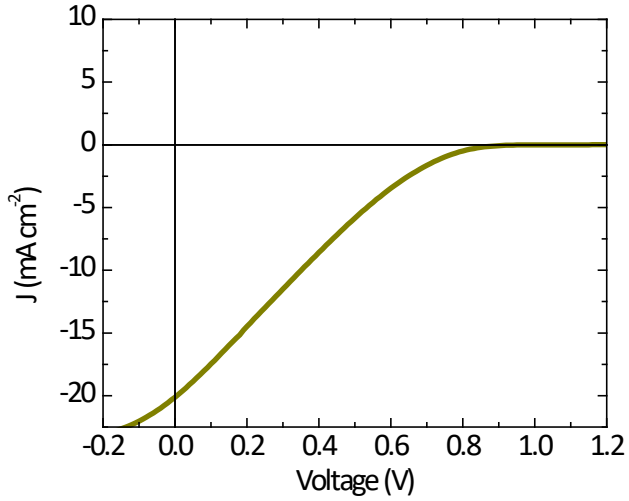

Fig. S3 J-V scan for a *p-i-n* device with the structure ITO/TaTm (40 nm)/$MAPbI_3$ (500 nm)/ C_{60} (40 nm)/Ag.

Table S1 Photovoltaic parameters for the main solar cells architecture studied. The effect of the selective removal of the intrinsic charge transport layers is highlighted.

	Device structure	V_{oc} (mV)	J_{sc} (mA cm^{-2})	FF (%)	PCE (%)
	TaTm/$MAPbI_3$/C_{60}	1041	20.12	16.8	3.5
	p-HTL/TaTm/$MAPbI_3$/C_{60}/n-ETL	1082	20.02	73.1	15.8
p-i-n	**p-HTL/**$MAPbI_3$/C_{60}/n-ETL	**1033**	20.19	73.3	15.3
	p-HTL/TaTm/$MAPbI_3$**/n-ETL**	1032	17.82	**45.0**	8.3
	n-ETL/C_{60}/$MAPbI_3$/TaTm/p-HTL	1115	20.28	79.8	18.0
n-i-p	**n-ETL/**$MAPbI_3$/TaTm/p-HTL	1084	20.45	**68.8**	15.2
	n-ETL/C_{60}/$MAPbI_3$**/p-HTL**	**998**	19.44	**68.7**	13.3

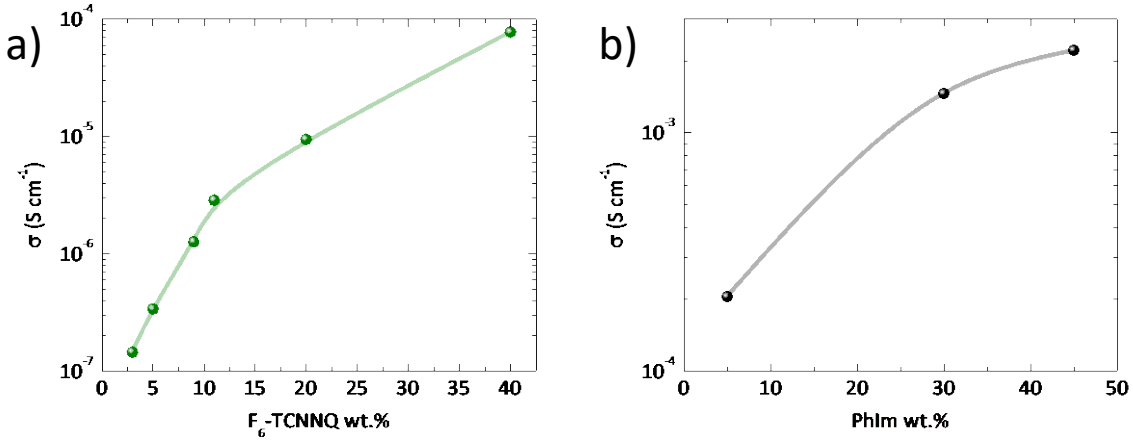

Fig. S4 Conductivity as a function of the dopant concentration for 100 nm thick films of (a) p-HTL (TaTm:F_6-TCNNQ) and (b) n-ETL (C_{60}:PhIm).

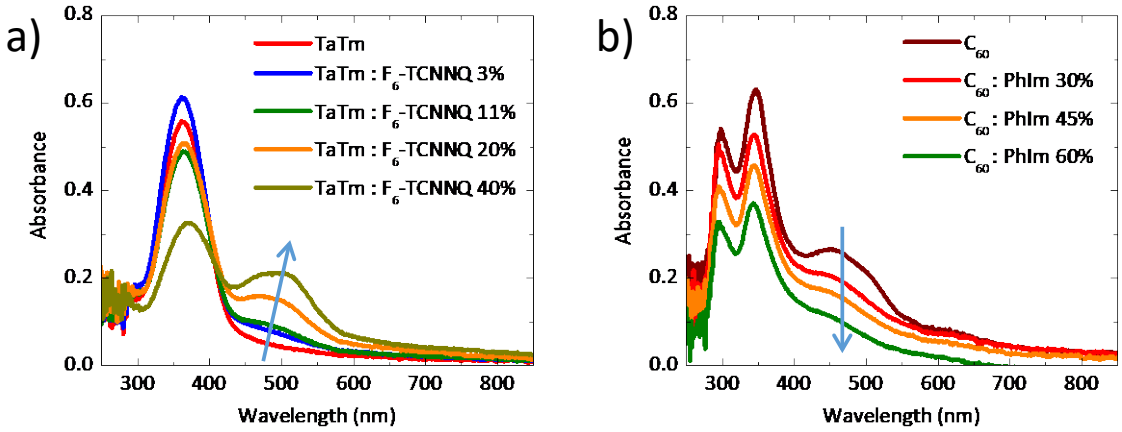

Fig. S5 Optical absorbance as a function of the dopant concentration for 40 nm thick films of (a) p-HTL (TaTm:F_6-TCNNQ) and (b) n-ETL (C_{60}:PhIm).

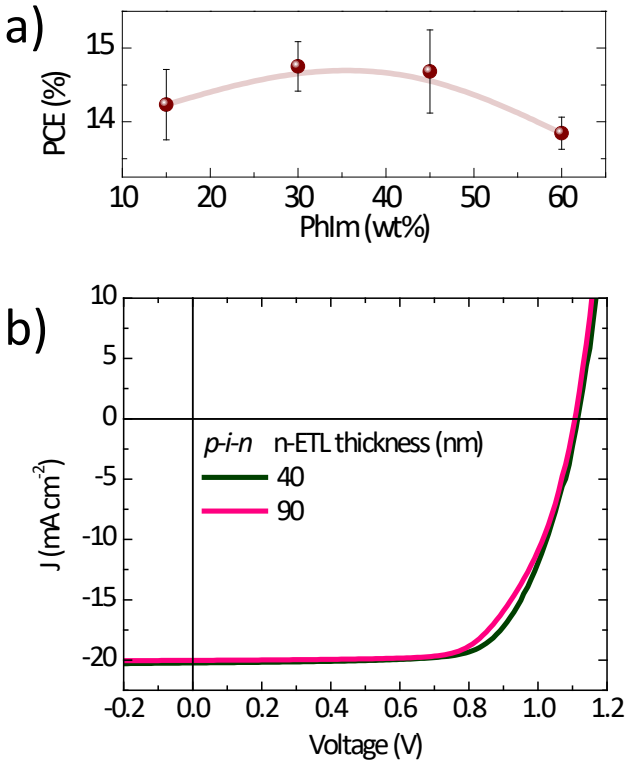

Fig. S6 (a) Trend of the PCE for a series of *p-i-n* cells with increasing concentration of the PhIm dopant in the n-ETL. (b) *J-V* scans for *p-i-n* devices with increasing thickness of the n-ETL (C_{60}:PhIm).

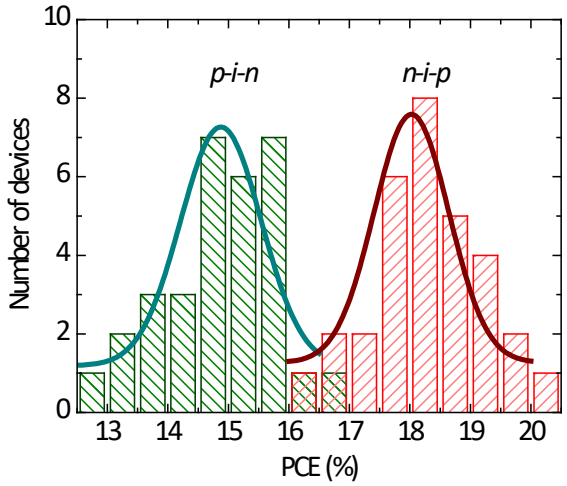

Fig. S7 Statistics of the PCE measured for *p-i-n* (green) and *n-i-p* devices (32 cells for each configuration). Green and red solid lines represent the Gaussian distribution fitting for the PCE.

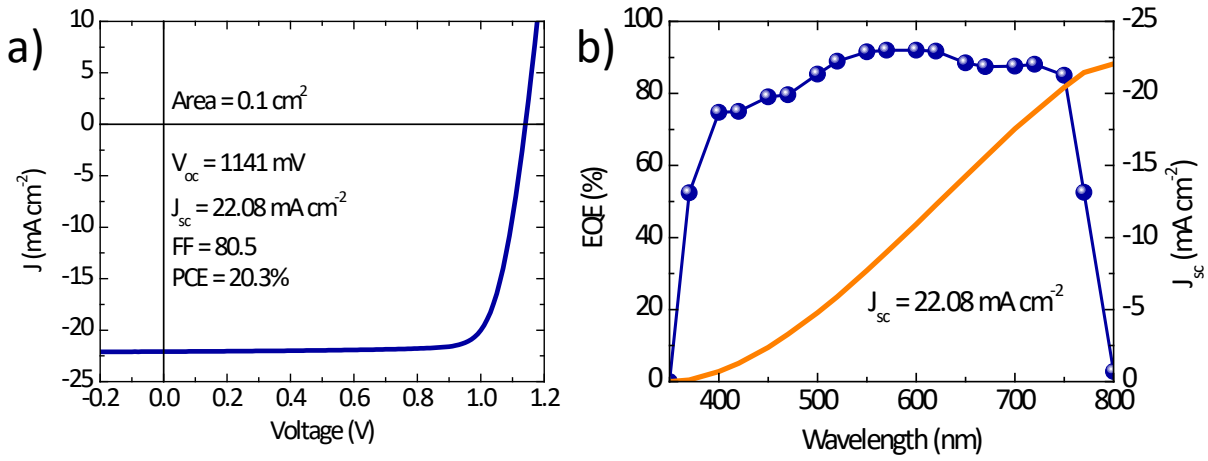

Fig. S8 (a) J-V curves under 100 mW cm^{-2} illumination and (c) EQE spectra (the integrated photocur-rent with the AM1.5G solar spectrum is shown on the right axis) for the top performing *n-i-p* perovskite solar cell.

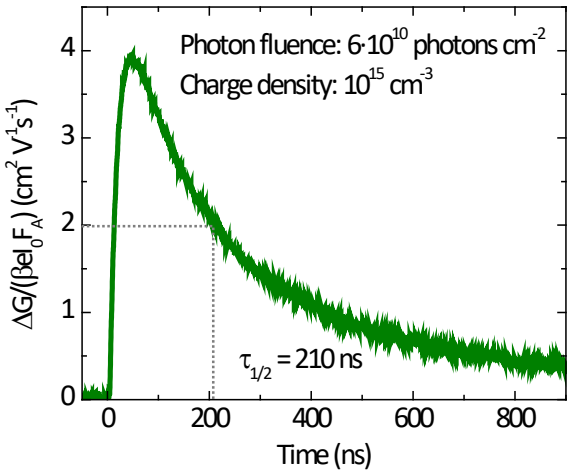

Fig. S9. TRMC trace for a 300 nm thick $MAPbI_3$ film recorded at excitation wavelengths of 650 nm with a fluence of $6 \cdot 10^{10}$ photons cm^{-2} per pulse, resulting in a charge density (10^{15} cm^{-3}) corresponding to 1 AM1.5. The extrapolation of the half lifetime t is shown for clarity.

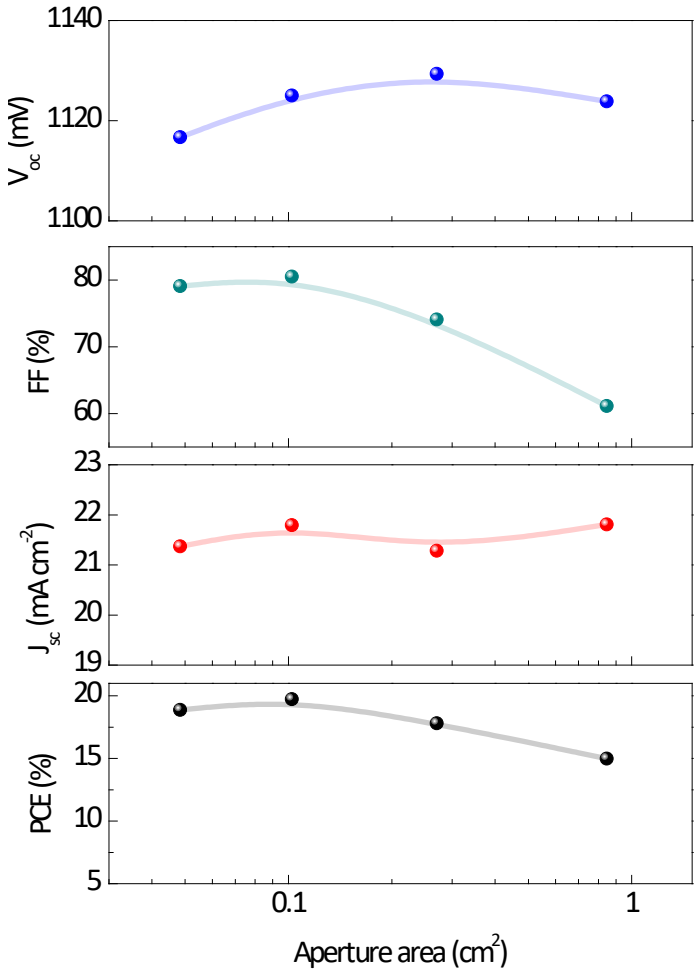

Fig. S10 Photovoltaic parameters extracted from *J-V* and EQE measurements for a series of *n-i-p* devices with increasing area, defined as the shadow mask aperture. Note that the area of the ITO/metal is also increasing proportionally.

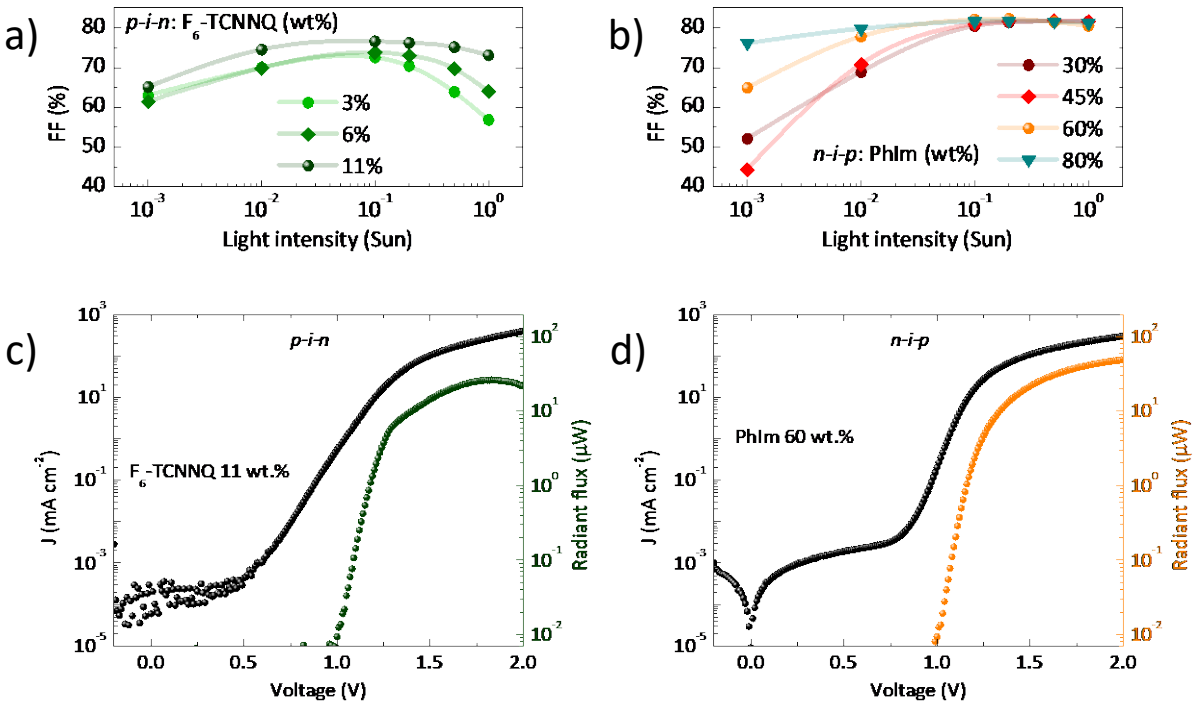

Fig. S11 Light intensity dependence of the measured *FF* for different doping concentration in the charge transport layer at the front contact for (a) *p-i-n* and (b) *n-i-p* cells. *J-V* and electroluminescence characteristics for the 2 reference (c) *p-i-n* and (d) *n-i-p* devices.

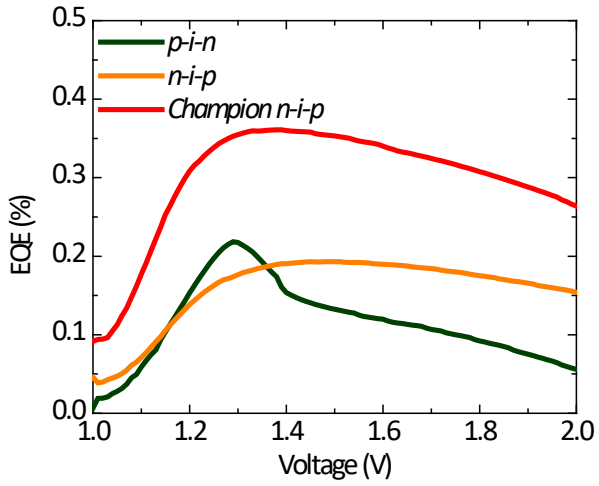

Fig. S12 EQE of electroluminescence for *p-i-n* and *n-i-p* cells. The EQE characteristic for our record PCE *n-i-p* device is shown for comparison.

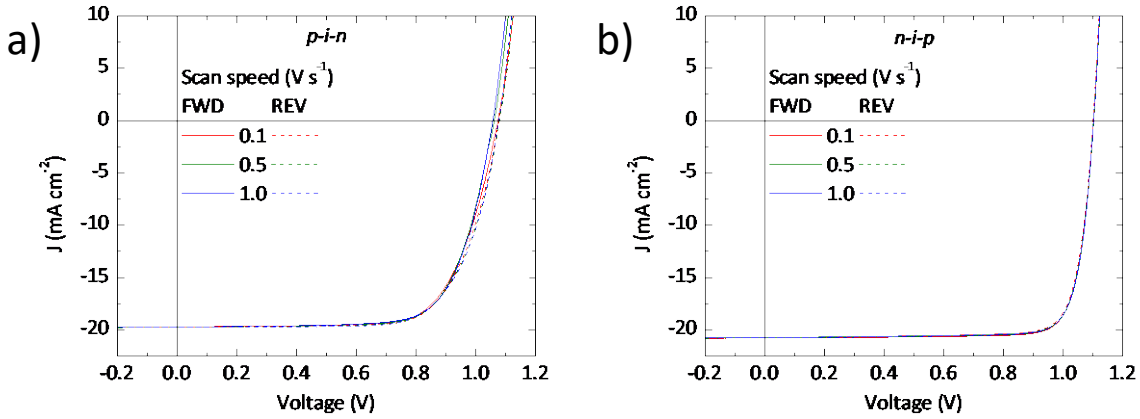

Fig. S13 Characterization of the *J-V* hysteresis of (a) *p-i-n* and (b) *n-i-p* perovskite solar cells, performed by measuring the current as a function of the bias scan direction at different scan speed.

Table S2 Photovoltaic parameters extracted from the *J-V* hysteresis (Fig. S12) for *p-i-n* and *n-i-p* perovskite solar cells, under forward (FWD) and reverse (REV) bias at different scan speed.

	Speed	**0.1 V s^{-1}**		**0.5 V s^{-1}**		**1.0 V s^{-1}**	
	Direction	FWD	REV	FWD	REV	FWD	REV
p-i-n	V_{oc} (mV)	1073	1076	1061	1077	1056	1075
	J_{sc} (mA cm^{-2})	19.65	19.64	19.65	19.65	19.63	19.65
	FF (%)	71.0	71.4	72.3	71.1	72.7	71.0
	PCE (%)	15.0	15.1	15.1	15.0	15.1	15.0
n-i-p	V_{oc} (mV)	1101	1100	1102	1101	1101	1102
	J_{sc} (mA cm^{-2})	20.73	20.73	20.73	20.73	20.73	20.73
	FF (%)	83.0	82.2	82.9	82.7	82.7	82.8
	PCE (%)	19.0	18.7	18.9	18.9	18.9	18.9

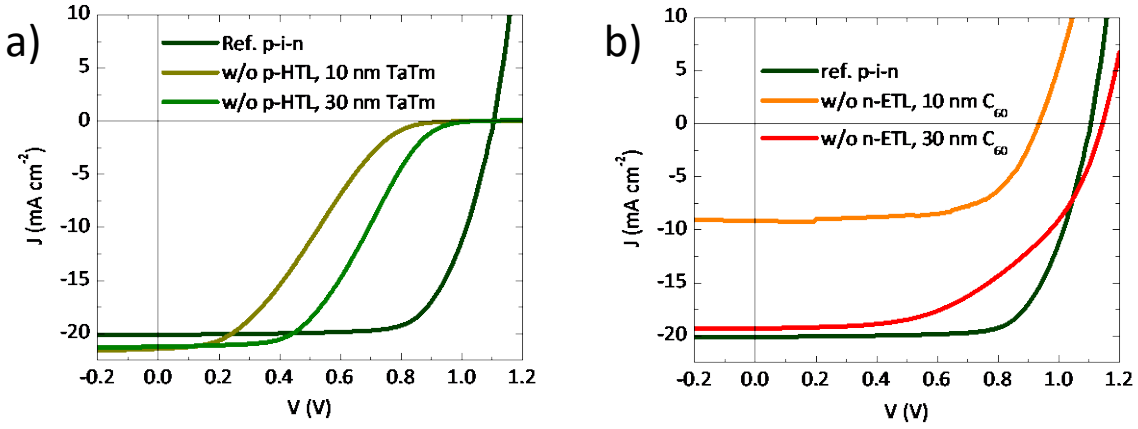

Fig. S14 *J-V* characteristics of *p-i-n* perovskite devices without the (a) p-HTL or the (b) n-ETL, for different thicknesses of the intrinsic TaTm and C_{60} transport layer, respectively.

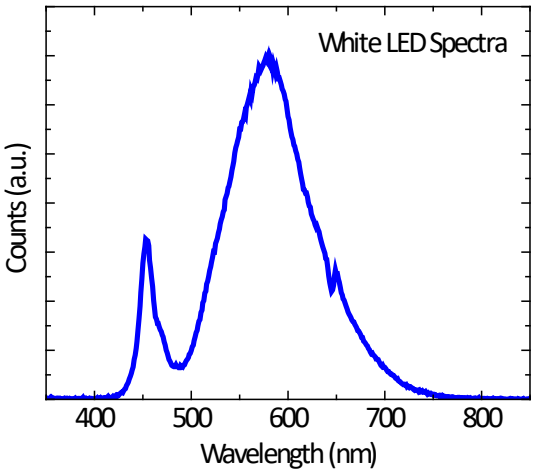

Fig. S15 Optical emission spectra of the white LED used to illuminate the solar cells during lifetime measurements.

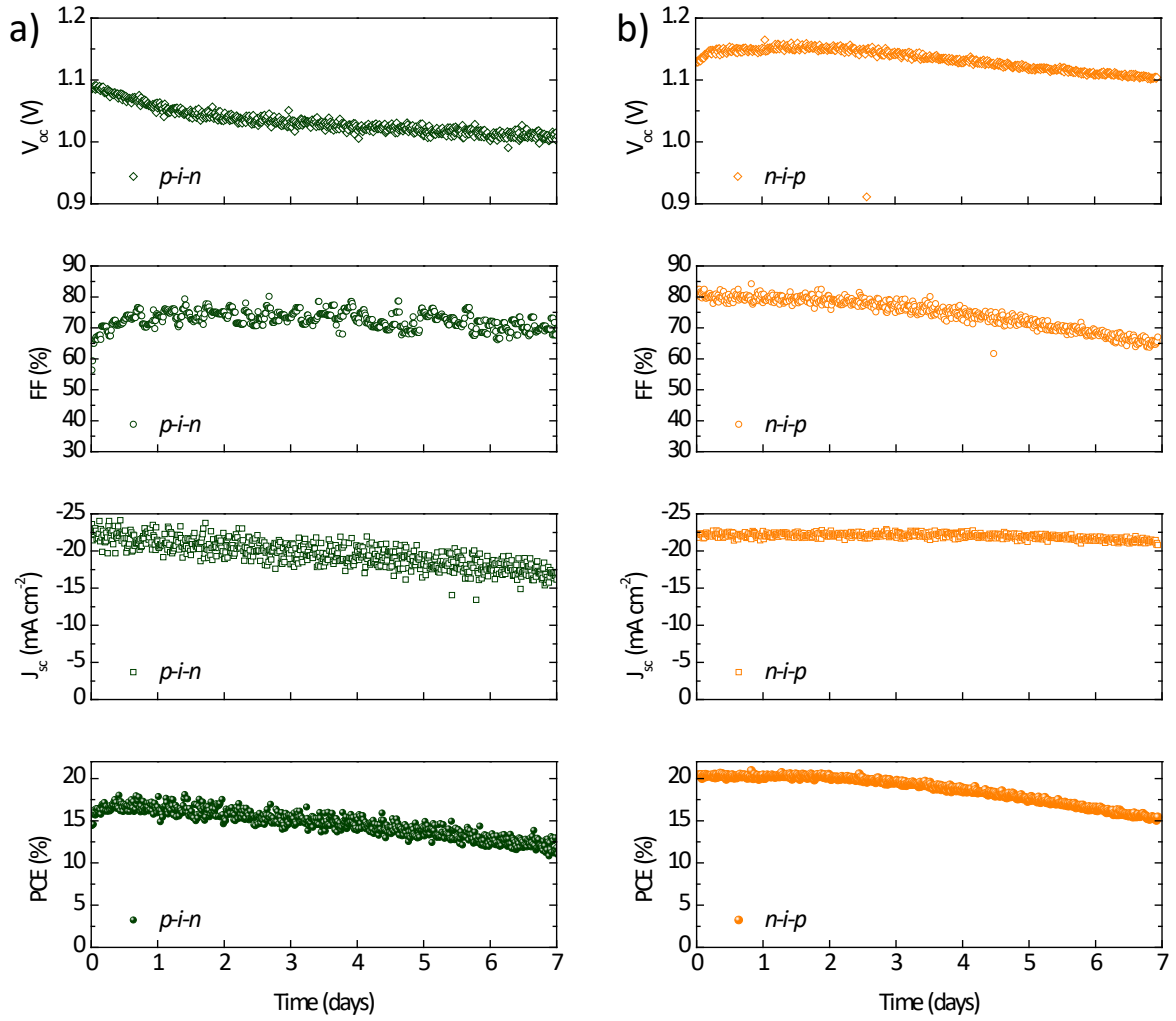

Fig. S16 Comparison of the lifetime of (a) *p-i-n* and (b) *n-i-p* perovskite devices. The photovoltaic parameters are extracted while the cells are kept under continuous illumination at short circuit conditions and with no temperature control.

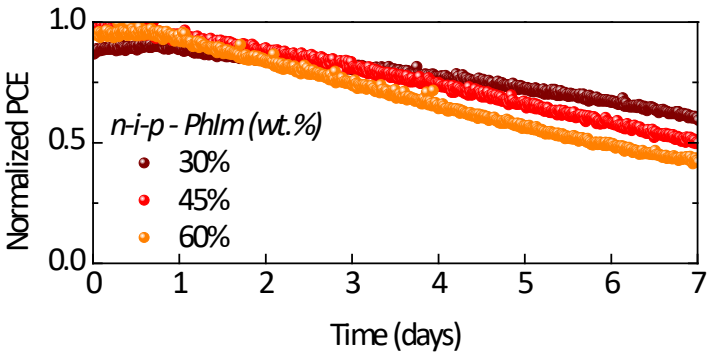

Fig. S17 Evolution of the PCE (normalized here for comparison) for a series of *n-i-p* solar cells with increasing concentration of the PhIm dopant in the n-ETL front contact.